Available online at www.sciencedirect.com

ScienceDirect

Advances in Space Research 59 (2017) 1568–1576

ADVANCES IN SPACE RESEARCH (a COSPAR publication)

www.elsevier.com/locate/asr

# Inferring electromagnetic ion cyclotron wave intensity from low altitude POES proton flux measurements: A detailed case study with conjugate Van Allen Probes observations

Yang Zhang [a,b], Run Shi [a,b,*], Binbin Ni [a,b,*], Xudong Gu [a,b], Xianguo Zhang [b], Pingbing Zuo [b], Song Fu [a], Zheng Xiang [a], Qi Wang [a], Xing Cao [a], Zhengyang Zou [a]

[a] Department of Space Physics, School of Electronic Information, Wuhan University, Wuhan, Hubei, China
[b] State Key Laboratory of Space Weather, National Space Science Center, Chinese Academy of Sciences, Beijing, China

Received 17 October 2016; received in revised form 29 November 2016; accepted 24 December 2016
Available online 31 December 2016

**Abstract**

Electromagnetic ion cyclotron (EMIC) waves play an important role in the magnetospheric particle dynamics and can lead to resonant pitch-angle scattering and ultimate precipitation of ring current protons. Commonly, the statistics of in situ EMIC wave measurements is adopted for quantitative investigation of wave-particle interaction processes, which however becomes questionable for detailed case studies especially during geomagnetic storms and substorms. Here we establish a novel technique to infer EMIC wave amplitudes from low-altitude proton measurements onboard the Polar Operational Environmental Satellites (POES). The detailed procedure is elaborated regarding how to infer the EMIC wave intensity for one specific time point. We then test the technique with a case study comparing the inferred root-mean-square (RMS) EMIC wave amplitude with the conjugate Van Allen Probes EMFISIS wave measurements. Our results suggest that the developed technique can reasonably estimate EMIC wave intensities from low-altitude POES proton flux data, thereby providing a useful tool to construct a data-based, near-real-time, dynamic model of the global distribution of EMIC waves once the proton flux measurements from multiple POES satellites are available for any specific time period.


*Keywords:* EMIC wave intensity; POES proton flux measurements; Van Allen Probes observations; Resonant wave-particle interactions; Precipitated-to-trapped proton flux ratio

## 1. Introduction

As one of the most intense electromagnetic wave modes in the Earth's magnetosphere, electromagnetic ion cyclotron (EMIC) waves generally exhibit discrete emissions occurring in distinct frequency bands which are separated by the multiple ion gyrofrequencies (Thorne, 2010). EMIC waves have been a topic of intense interest due to the important roles that they play in the magnetospheric particle dynamics (e.g., Thorne and Horne, 1992; Horne and Thorne, 1997). Their generation is closely associated with the anisotropic distributions of ring current protons (e.g., Kennel and Petschek, 1966; Roux et al., 1982; Anderson et al., 1992; Wang et al., 2016). Based on observations and simulations, it is proposed that EMIC waves are excited when plasma sheet energetic ions are injected into the ring current during magnetic substorms (e.g., Cornwall, 1965; Criswell, 1969) and are enhanced during geomagnetic storms (e.g., Jordanova et al., 2008; Fraser et al., 2010). Scattering by EMIC waves can cause ultimate

* Corresponding authors at: Department of Space Physics, Wuhan University, China.
*E-mail addresses:* runshi@whu.edu.cn (R. Shi), bbni@whu.edu.cn (B. Ni).

http://dx.doi.org/10.1016/j.asr.2016.12.035
0273-1177/

atmospheric precipitation losses of both ring current protons and radiation belt relativistic electrons (e.g., Summers et al., 2007; Ni et al., 2015; Cao et al., 2016). A number of studies have evaluated the rates of EMIC wave induced pitch angle diffusion based on quasi-linear theory (Loto'aniu et al., 2006; Ukhorskiy et al., 2010) or test particle simulations (Albert and Bortnik, 2009; Liu et al., 2010). It is demonstrated that EMIC waves are capable of diffusing relativistic (> MeV) electrons and low-energy (~10–100 keV) protons on timescales of hours or less, approaching the regime of strong diffusion. In fact, accurate quantification of the effect of EMIC waves on the magnetospheric particle dynamics requires detailed information of background parameters, including the ambient magnetic field and plasma density, wave amplitude, wave frequency spectrum, wave normal angle distribution, wave latitudinal coverage, and wave local time coverage. The MLT extent of EMIC waves is not necessary for bounce-averaged diffusion coefficient calculations, but can be significantly important when evaluating the drift- and bounce-averaged rates of scattering rates, especially for relativistic electrons that drift around the Earth within a few minutes.

However, in situ wave measurements are unavoidably limited over time and space. In order to deal with this issue, a novel methodology has been developed, on basis of a causal connection between wave intensity in the equatorial region and the precipitated-to-trapped flux ratio at low altitudes (Li et al., 2013; Ni et al., 2014; De Soria-Santacruz et al., 2015). A data-based, dynamic global model of whistler mode waves was established using low altitude satellite (e.g., POES) electron data. Their method has been validated with instantaneous wave measurements from approximately conjugate Van Allen Probes and the model results showed reasonable agreement. A number of recent studies have used their methodology to construct the global distribution of chorus waves to improve understanding of the roles of wave-particle interactions in the radiation belt electron dynamics (Thorne et al., 2013; Xiao et al., 2015). However, no work has been done to infer EMIC wave intensity from low altitude POES proton flux measurements, while a similar causation also exists between EMIC wave induced scattering and proton precipitation loss. Therefore, the present study is directed toward building up such a physical correlation based on careful observational and numerical investigation of a Van Allen Probes and POES conjunction event. In addition, we quantitatively evaluate the consequence of proton loss due to EMIC wave scattering.

The remainder of the paper is outlined as follows: in Section 2 we give a brief description of the satellite data and the methodology that can connect the EMIC wave intensity and proton precipitated-to-trapped flux ratio. In Section 3 the satellite conjunction event of our interest is illustrated, followed by a detailed analysis to evaluate the EMIC wave amplitude from the POES proton data and the quantitative validation with conjugate Van Allen Probes wave measurements. We discuss our results and summarize the conclusions in Section 4.

## 2. Data and methodology

In the present study the proton measurements from multiple low-altitude POES satellites are used to infer the amplitude of the EMIC waves, and simultaneous conjugate wave observations from Van Allen Probe A are adopted to testify the model results.

The NOAA POES mission consists of a series of satellites that orbit at the altitude of ~800 km with extended coverage over a broad range of MLT and $L = \sim 2$–8 around every ~100 min. We use the proton flux data from the NOAA POES satellites and EUMETSAT MetOp satellites. The Space Environment Monitor-2 (SEM-2) instrument package onboard these POES satellites that provides us the particle information includes the Medium Energy Proton and Electron Detector (MEPED) with two solid-state particle detector telescopes (0° and 90°) capable of monitoring protons in six energy bands (30–80 keV, 80–240 keV, 240–800 keV, 800–2500 keV, 2500–6900 keV, and >6900 keV) (Evans and Greer, 2004). The 0° detector has a field view of ±15° centered along the local zenith. It measures the precipitating particle fluxes inside the bounce loss cone at $L > 1.4$ (Rodger et al., 2010). The other detector that is perpendicular to the former with the same field of view measures trapped and quasi-trapped particles over the invariant latitude range between 55° and 68° ($\sim L = 3 \sim 7$ in a dipole field) (Meredith et al., 2011).

The dual-spacecraft Van Allen Probes mission with a perigee of ~1.1 $R_E$ and apogee of 5.8 $R_E$, was launched on 30 August 2012. Both probes (A and B) follow a low inclination (~10°) with an orbital period of ~9 h. The Electric and Magnetic Field Instrument Suite and Integrated Science (EMFISIS) suite onboard Van Allen Probes provides high temporal resolution (64 vectors per second) magnetic field measurement. In this study we use the triaxial fluxgate magnetometer (MAG) on the EMIFISIS instrument to acquire the intensity of EMIC waves. We process the data through fast Fourier transform (FFT) technique and then calculate the wave power. The upper hybrid resonance frequency, which is inferred from electric field spectral measurements from The EMFISIS High Frequency Receiver (HFR), is used to calculate the plasma density (Kurth et al., 2015).

The POES proton data are used to infer the amplitude of EMIC waves, since EMIC waves are expected to preferentially resonate with ring current protons at these energies (e.g., Summers, 2005; Cao et al., 2016). We focus on two energy channels, i.e., 30–80 keV and 80–240 keV, and two telescopes (0° and 90°). The two telescopes measure the proton count rates inside the loss cone and outside the loss cone respectively (e.g., Lam et al., 2010; Li et al., 2013; Ni et al., 2014). The key parameter of our investigation is the ratio between precipitating and trapped proton fluxes,

which can be computed theoretically from the following equations (Li et al., 2013; Ni et al., 2014):

$$CR(E_1 < E < E_2)|_{0^\circ} = \int_{E_1}^{E_2}\int_0^{2\pi}\int_0^{\beta} \frac{S(E)}{\langle D_{\alpha\alpha}\rangle|_{LC}\cos\alpha_{eq,in}} \frac{I_0\left(\frac{\alpha_{eq,in}}{\alpha_{LC}}z_0\right)}{z_0 I_1(z_0)} A \times \sin\eta d\eta d\psi dE, \quad (1)$$

$$CR(E_1 < E < E_2)|_{90^\circ} = \int_{E_1}^{E_2}\int_0^{2\pi}\int_0^{\beta} \times \frac{S(E)}{\langle D_{\alpha\alpha}\rangle|_{LC}\cos\alpha_{eq,out}} \left[\frac{I_0(z_0)}{z_0 I_1(z_0)} + \ln\frac{\sin\alpha_{eq,out}}{\sin\alpha_{LC}}\right] A \times \sin\eta d\eta d\psi dE, \quad (2)$$

$$R = \frac{CR(E_1 < E < E_2)|_{0^\circ}}{CR(E_1 < E < E_2)|_{90^\circ}}, \quad (3)$$

where $CR|_{0^\circ}$ and $CR|_{90^\circ}$ are the proton count rates measured by the 0° and 90° telescopes respectively. $E$ is the particle energy, and $E_1$ and $E_2$ are the lower and upper cutoff energy of the energy channel. $\beta$ is the field of view of the telescope with the value of 15°. $S(E)$ represents the proton energy spectrum. $\langle D_{\alpha\alpha}|_{LC}\rangle$ is the bounce-averaged particle pitch angle scattering coefficient at the equatorial bounce loss cone. $Z_0$ is a function of particle kinetic energy $E$ and related to $\langle D_{\alpha\alpha}|_{LC}\rangle$: $Z_0 = \sqrt{\frac{2D_{SD}}{\langle D_{\alpha\alpha}|_{LC}\rangle\cos\alpha_{eq}}}$, where $D_{SD}$ is the strong diffusion rate which is energy dependent. The parameters $\alpha_{eq,in}$ and $\alpha_{eq,out}$ are the equatorial particle pitch angles inside and outside the loss cone. $I_0$ and $I_1$ are the modified Bessel functions. $A$ is the detector area, $\eta$ and $\psi$ are defined in Fig. 1 of Ni et al. (2014) in relation to the geometry of the POES MEPED detector. Eqs. (1)–(3) demonstrate that the ratio $R$ is one-to-one related to $\langle D_{\alpha\alpha}|_{LC}\rangle$, which varies essentially with wave amplitude. Therefore, given $R$-value, it is feasible to infer the amplitude of plasma waves responsible for particle precipitation loss through inversion.

Before applying the above method, it is necessary to make several assumptions. Firstly, the proton energy spectrum $S(E)$ needs to be defined. We follow Xiao et al. (2012) to adopt a kappa-type distribution of ring current protons:

$$S(E) \sim \frac{p^2\Gamma(\kappa+l+1)}{\pi^{3/2}\theta^3\kappa^{(l+3/2)}\Gamma(l+1)\Gamma(\kappa-1/2)}\left(\frac{p\sin\alpha_e}{\theta}\right)^{2l} \cdot \left[1+\frac{p^2}{\kappa\theta^2}\right]^{-(\kappa+l+1)}, \quad (4)$$

where $l$ indicates the loss cone index, $\kappa$ represents the spectral index, $\Gamma$ is the gamma function, $P$ is the proton momentum (normalized by $m_pc$, where $m_p$ is the proton mass), $\theta^2$ stands for the thermal parameter scaled by the proton rest mass energy $m_pc^2$ (~938 MeV), and $\alpha_e$ means the equatorial pitch angle. Here we choose the representative values of the parameters as $l = 0.01$, $\kappa = 3$, $\alpha_e = 90^\circ$ and $\theta^2 = 10^{-5}$ to establish the proton energy spectrum (Xiao et al., 2012) for further calculations. Secondly, the background cold plasma density is inferred from the upper hybrid resonance frequency line extracted from the Van Allen Probes EMFISIS HFR measurements (Kurth et al., 2015) and is also assumed constant over the latitudinal extent of wave presence, which is taken as within 40° of the geomagnetic equator in this study. Thirdly, to calculate proton scattering rates by EMIC waves as a function of wave amplitude, we follow previous studies (e.g., Glauert and Horne, 2005; Summers et al., 2007; Ni et al., 2015; Cao et al., 2016) to assume that the wave spectral intensity follows a typical Gaussian distribution determined by a center normalized frequency $f_m$, a normalized bandwidth $\delta_f$, and a frequency range between $f_1$ and $f_2$. A dipolar geomagnetic field is also adopted to compute bounce-averaged diffusion coefficients.

Following the study of Ni et al. (2014), the general procedure adopted to infer EMIC wave intensities is outlined as follows. Firstly, depending on the $L$-shell location, we set up the respective threshold values for the 30–80 keV and 80–240 keV proton channels to avoid the contamination from the background noise. We also remove the data points inside the South Atlantic anomaly to minimize the effect of the drift loss cone. Secondly, we compute the bounce averaged proton pitch angle scattering rates at the equatorial loss cone, for the energy range that covers both proton channels, as a function of EMIC wave amplitude. Together with the proton strong diffusion rates, we evaluate the value of the ratio ($R$, Eq. (3)) for the two proton channels as a function of EMIC wave amplitude. Finally, we infer two values of EMIC wave amplitude (corresponding to the two energy channels) by interpolating POES observed ratios of precipitated to trapped proton fluxes.

## 3. Analysis results

Through pursuing rough conjunctions with the bin size of ~0.5 h × 0.5 $L$ × 0.5 MLT (e.g., Li et al., 2013; Ni et al., 2014), the present study focuses on a conjunction event between the POES NOAA-19 spacecraft and Van Allen Probe A around 18:30–19:00 UT on 22 March 2013. The model results of EMIC wave intensity inferred from the POES proton flux data will be quantitatively validated with the high-quality wave measurements from Van Allen Probe A to check the applicability of our proposed methodology described in Section 2.

Fig. 1 displays the overall picture of Van Allen Probe A observed EMIC waves and NOAA-19 observed proton fluxes during the selected rough conjunction event. Fig. 1 (a)–(c) present the magnetic field spectral intensities below 10 Hz obtained from the fast Fourier transform analysis of MAG data, corresponding wave ellipticity, and corresponding wave normal angles computed using the singular value decomposition method (Santolík et al., 2003). The

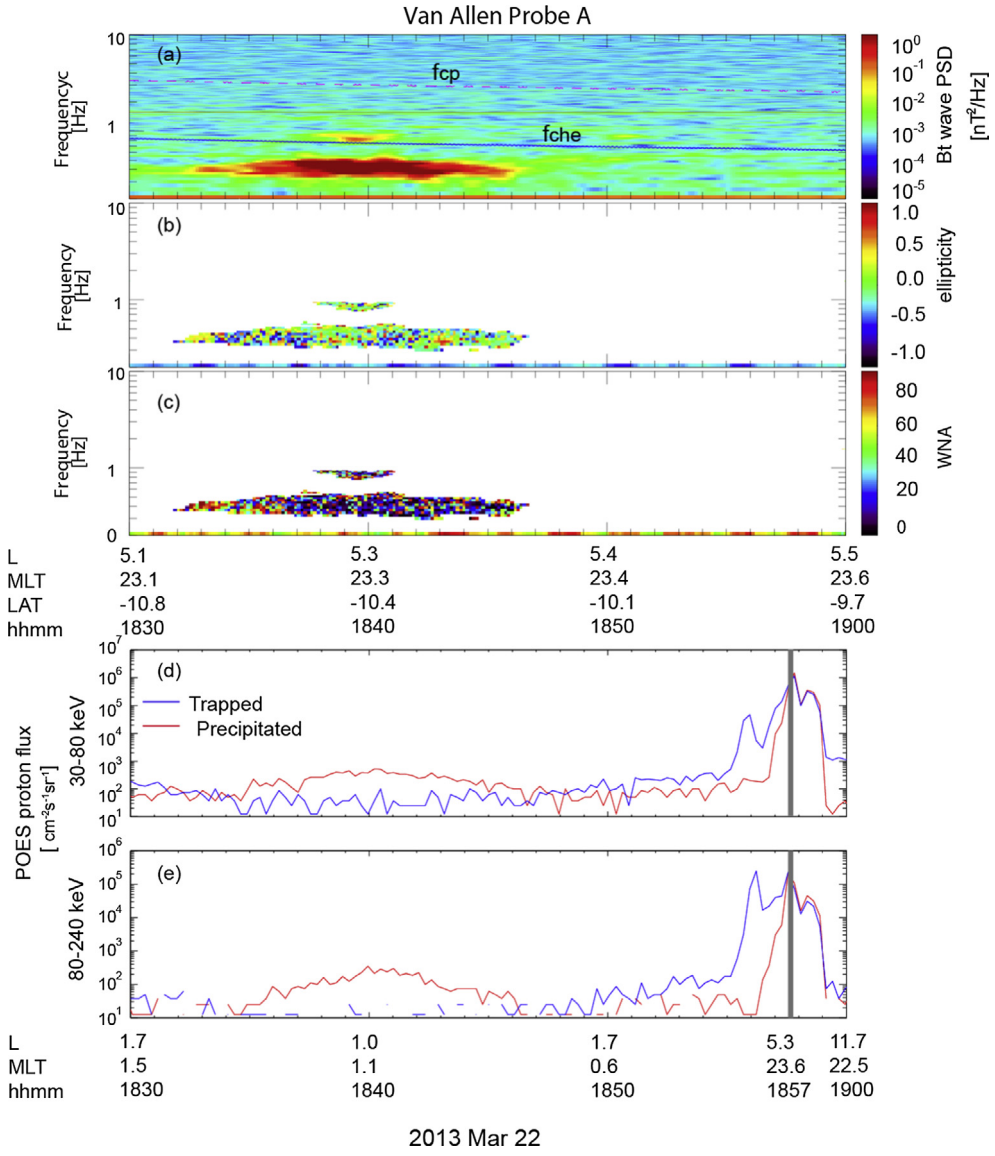


Fig. 1. The conjunction event between POES-19 and Van Allen Probe A on 22 March 2013. (a–c) Magnetic field power spectral intensity, wave ellipticity, and wave normal angle of EMIC waves observed by Van Allen Probe A. (d and e) Trapped and precipitated proton fluxes measured by POES-19 for the two energy channels of 30–80 keV and 80–240 keV. The shaded time interval denotes the close conjunction period between the two satellites.

purple dotted and blue solid lines in the top panel denote the local proton gyrofrequency ($f_{cp}$) and the helium ion gyrofrequency ($f_{cHe}$) respectively. Two bands of EMIC waves, i.e., $H^+$ band and $He^+$ band, occurred during the period of interest. The weak $H^+$ band emissions lasted for about 3 min, and the much stronger $He^+$ band waves lasted for about 10 min. The principally left-handed polarized waves propagated primarily along the field line or at small wave normal angles ($<\sim 10°$). In the subsequent analysis we focus on the $He^+$ band EMIC waves due to its dominance over the wave power. Fig. 1(d) and (e) shows the NOAA-19 measured fluxes of trapped (blue curves) and precipitated (red[1] curves) protons for 30–80 keV and 80–240 keV respectively. The shaded region in each panel denotes the conjunction between NOAA-19 and Van Allen Probe A when the locations of two satellites were at the same $L$ shell and MLT bin. It is clearly seen that there occurred a sharp increase in the precipitated and trapped fluxes and the ratio between them as well during the conjunctive time period of EMIC wave activity.

As indicated in Fig. 1, the approximate conjunction occurred at $L \sim 5.3$ around the local midnight. To avoid the contamination from the background noise, in the following analysis we select 1000 c/s and 100 c/s as the respective threshold values of the trapped proton count rates for the 30–80 keV and 80–240 keV energy channels, following previous studies (Li et al., 2013; Ni et al., 2014). In addition, we take the following parameter values to represent the Gaussian distribution of $He^+$ band EMIC wave

[1] For interpretation of color in Fig. 1, the reader is referred to the web version of this article.

frequency spectrum at $L \sim 5$: the lower and upper cutoff frequencies $f_1 = 0.08 f_{cp}$ and $f_2 = 0.20 f_{cp}$, the bandwidth $\delta_f = (f_2 - f_1)/4$, and the peak wave frequency $f_m = (f_1 + f_2)/2$. The ambient plasma density is set as 75.4 $cm^{-3}$ from the upper hybrid resonance frequency line. With all the above information available, we can then calculate bounce-averaged proton pitch angle diffusion rates at the equatorial loss cone due to field-aligned $He^+$ band EMIC waves, $\langle D_{\alpha\alpha}|_{LC}\rangle$, for the proton energy range of 30–240 keV. We obtain the matrix of quasi-linear $\langle D_{\alpha\alpha}|_{LC}\rangle$ of 1 nT EMIC waves following Summers (2005) and Summers et al. (2007) and quantify the energy-dependent strong diffusion rate $D_{SD}$ following Summers and Thorne (2003). Fig. 2 illustrates the comparison between $\langle D_{\alpha\alpha}|_{LC}\rangle$ and $D_{SD}$ at $L = 5.3$ and MLT = 23.6. Fig. 2(a) shows $\langle D_{\alpha\alpha}|_{LC}\rangle$ as a function of proton kinetic energy for three specific wave amplitudes of 100 pT, 300 pT, and 1000 pT. As the $He^+$ band wave intensity increases, $\langle D_{\alpha\alpha}|_{LC}\rangle$ approaches $D_{SD}$. When the amplitude reaches 1000 pT, the diffusion rates exceed the strong diffusion rate at lower proton energies. Fig. 2(b) clearly shows that for specific proton energy we can identify an EMIC amplitude for which $\langle D_{\alpha\alpha}|_{LC}\rangle$ equals $D_{SD}$. In general, $D_{SD}$ increases with the proton kinetic energy, while $\langle D_{\alpha\alpha}|_{LC}\rangle$ decreases with the proton kinetic energy. As a result, the EMIC amplitude required for strong diffusion is 830 pT for 30 keV protons, 1180 pT for 80 keV protons, and ~2 nT for 240 keV protons in the regime of quasi-linear diffusion. It means that for a given wave frequency distribution, less intense EMIC wave activity is needed to scatter ring current protons to fill the loss cone for the 30–80 keV channel than for the 80–240 keV channel.

The ratio $R$ is derived based on the equations in Section 2 once $\langle D_{\alpha\alpha}|_{LC}\rangle$ and $D_{SD}$ are known for illustration as a curve in the (Bw, $R$)-space. Through linear interpolation over such a theoretical curve, we can obtain two inferred EMIC wave amplitudes corresponding to observed precipitated-to-trapped flux ratios of two energy channels. Fig. 3 shows the modeled $R$-value curves as a function of EMIC wave amplitude for the 30–80 keV and the 80–240 keV channel, respectively. For the conjunction event we use the POES data at 18:57 UT to infer the corresponding wave amplitude when NOAA 19 was located at $L = 5.3$ and MLT = 23.6. The observed count rates of the precipitated and trapped electron population were 236 c/s and 1398 c/s for the 30–80 keV proton channel, 60 c/s and 440 c/s for the 80–240 keV proton channel. The ratio of the count rate was 0.1691 and 0.1362 for the two energy channels, respectively. We then interpolate through the theoretical curves for the above observed $R$-values to get two

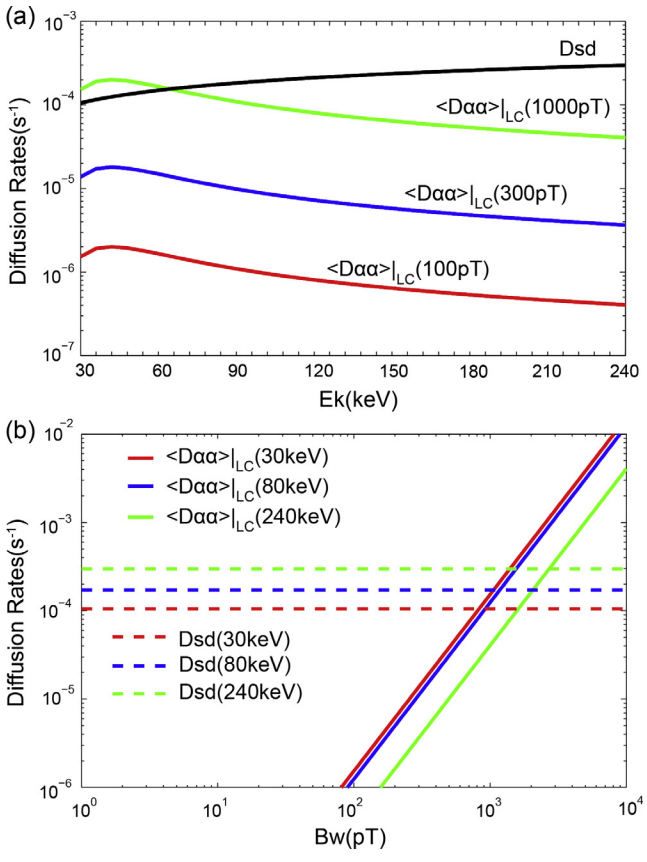


Fig. 2. For $L = 5.3$ and MLT = 23.6, (a) bounce-averaged pitch angle diffusion rates at the equatorial loss cone $\langle D_{\alpha\alpha}|_{LC}\rangle$ as a function of proton kinetic energy for three specific wave amplitudes of 100 pT, 300 pT and 1000 pT and their comparisons with the strong diffusion rate $D_{SD}$; (b) $\langle D_{\alpha\alpha}|_{LC}\rangle$ as a function of EMIC wave amplitude for three specific proton energies of 30 keV, 80 keV, 240 keV and their comparisons with $D_{SD}$.

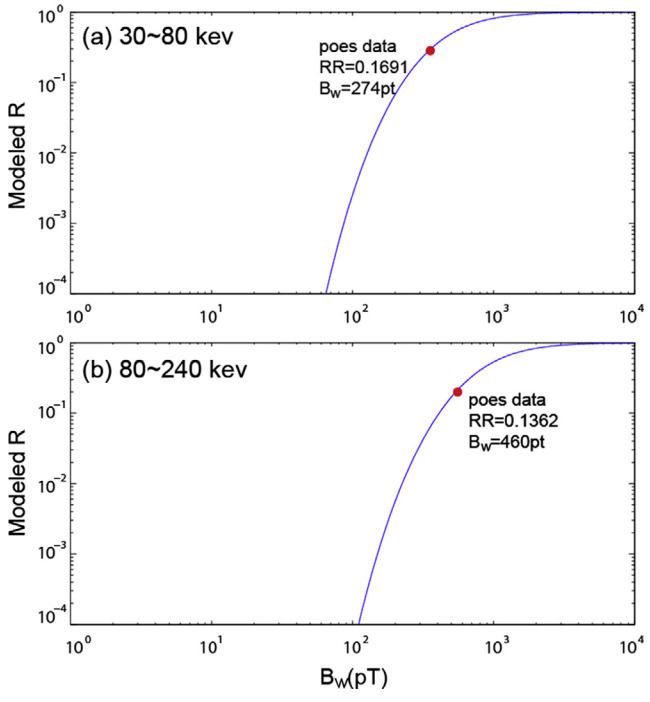


Fig. 3. Theoretical curves of the precipitated to trapped proton flux ratio as a function of EMIC wave amplitude for the (a) 30–80 keV channel and (b) 80–240 keV channel. The red solid circle signs shown in the curve stand for the inferred intensity using one specific POES data point by interpolation. (For interpretation of the references to color in this figure legend, the reader is referred to the web version of this article.)

wave amplitudes, i.e., 274 pT for the 30–80 keV channel and 460 pT for the 80–240 keV channel, respectively. Ideally, the EMIC wave amplitude inferred from the two energy channels should be identical. While there is a factor of 1.7 between the two inferred wave amplitudes, such a difference is tolerable with all the adopted assumptions taken into account. We defer to the discussions of uncertainties associated with the model results in Section 4.

We further apply our methodology to a longer time period when more MLTs can be covered at a certain range of $L$ shell. This is feasible due to the short orbital period (~100 min) and the multiple-probe availability of POES satellites. We consider a half-hour time interval (1830 UT–1900 UT) shown in Fig. 1 for subsequent comparisons with the EMFISIS wave observations. Fig. 4 illustrates the trajectories of the available six POES satellites and Van Allen Probe A in the $x$–$y$ plane of the solar magnetic coordinates. As indicated, the POES satellites orbited over a broad range of MLT and $L$ shell even within half an hour. During the same time period, Van Allen Probe A moved toward midnight at ~23–24 MLT. Here we focus on the spatial range of $L = 5.1$–$5.5$ and MLT = 20–24. We first synthesize the proton flux data from all the six POES satellites and then select all the effective proton data points over the space and time domain of interest to infer EMIC wave intensities one by one. Fig. 5 presents our results during the specific 0.5-h period between 18:30 UT and 19:00 UT on 22 Mar 2013. During the time of interest, three data points from POES satellites are useful to estimate the EMIC wave amplitudes. We define a useful data point as that the observed precipitated-to-trapped electron flux ratio is smaller than 1, since precipitated fluxes cannot exceed trapped fluxes for given energy or energy channel. The precipitated and trapped electron count rates and their ratios during the half hour are shown in Fig. 5(a) and (b) for the 30–80 keV energy channel, and in Fig. 5 (d) and (e) for the 80–240 keV electron channel. Corresponding to the ratio variation from 0.16 to 0.19 for the 30–80 keV energy channel, Fig. 5(c) presents the inferred EMIC wave amplitudes that vary from 223 pT to 274 nT with a root-mean-square (RMS) amplitude of 245 pT (red solid line). Similarly, Fig. 5(f) shows the inferred EMIC wave intensities with a RMS wave amplitude of 487 pT (blue solid line) for the 80–240 keV energy channel. As displayed in Fig. 5(g), the observed instantaneous EMIC wave intensities vary from 30 pT to 1380 pT, and the corresponding observed RMS amplitude calculated from the selected spatio-temporal interval is 328 pT. Therefore, the modeled average amplitude result during the considered 0.5-h interval, inferred using the 30–80 keV channel, is in good agreement with the average amplitude value from the satellite measurements during the same interval, while the averaged result from the 80–240 keV is somehow larger. In other words, for a given ($L$, MLT)-bin, in order to increase the reliability of inferred EMIC wave amplitudes, a reasonable interval of time resolution should be selected to produce reliable model results to represent the average wave amplitude feature over the period defined by the time resolution, which means that our method can only provide a near-real-time other than real-time inversion of the global distribution of EMIC wave intensity.

## 4. Discussions and conclusions

In the present study we have developed a novel technique, following the study of Ni et al. (2014), to infer the intensity of EMIC waves from low-altitude POES proton flux observations in terms of the precipitated-to-trapped

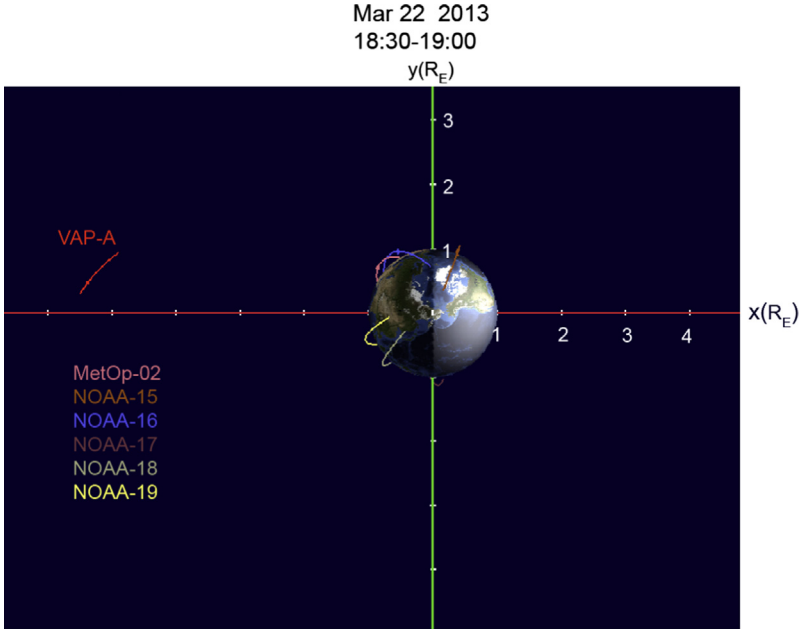


Fig. 4. Trajectories of the six POES satellites and the Van Allen Probe A spacecraft for the considered 0.5 h period during 18:30–19:00 UT on 22 Mar 2013.

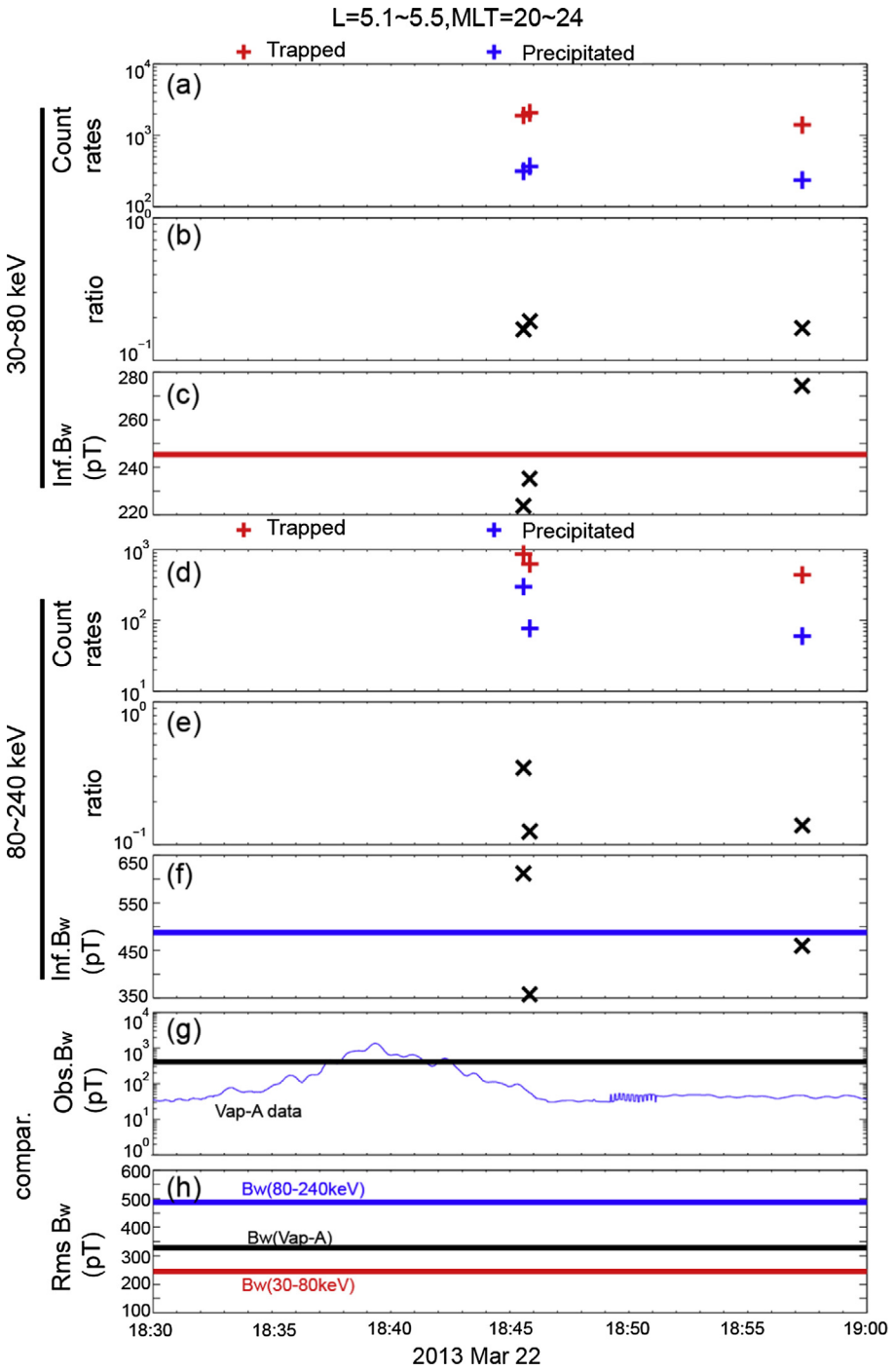


Fig. 5. EMIC wave amplitude analysis for the spatial region of $L = 5.1–5.5$ and MLT = 20–24 during 18:30–19:00 UT on 22 Mar 2013. (a–c) The count rates of trapped protons (red plus signs) and precipitated protons (blue plus signs), the ratio $R$ and the inferred EMIC wave amplitudes for the 30–80 keV channel; (d–f) The same as figure a–c but for 80–240 keV channel. (g) Van Allen Probe A EMFISIS observed instantaneous EMIC wave intensities curve. (h) Comparisons of observed and inferred RMS amplitude of the EMIC wave. (For interpretation of the references to color in this figure legend, the reader is referred to the web version of this article.)

electron flux ratio. It turns out that the method is feasible to assess the activities of EMIC waves, in addition to those of whistler-mode chorus and hiss (Thorne et al., 2013; Li et al., 2013; Ni et al., 2014; De Soria-Santacruz et al., 2015). Commonly, the statistics of in situ EMIC wave measurements is adopted for quantitative investigation of wave-particle interaction processes, which however becomes questionable for detailed case studies especially during geomagnetic storms and substorms. Therefore, our results suggest that the developed technique can reasonably estimate EMIC wave intensities from low-altitude POES proton flux data, thereby providing a useful

tool to construct a data-based, near-real-time, dynamic model of the global distribution of EMIC waves once the proton flux measurements from multiple POES satellites are available for any specific time period. Ideally, inferring the EMIC wave intensity from the precipitated and trapped proton fluxes should be independent of the wave measurements by equatorial satellites. But the presented method has used the direct measurements of EMIC wave frequency spectrum to infer EMIC wave amplitude, which adds a limit on the application of our technique, since proton scattering by EMIC waves is strongly affected by the assumption on EMIC wave frequency spectrum. Such a sensitivity analysis of inferred EMIC wave intensity to adopted wave frequency spectrum is left as a part of a comprehensive parametric study under way. In addition, we note that EMIC waves within different frequency bands resonate with different energy protons near their loss cone angles. Since the proton flux measurements by POES are available for multiply energy channels, it can make it possible to reconstruct EMIC wave intensities at different frequency bands based on the precipitated-to-trapped flux ratios for different energy channels. The inferred EMIC wave frequency spectrum (independent of the direct wave measurements) and wave amplitude can be approximately regarded as the summation of EMIC wave intensities at different frequency bands. It is also worthwhile to point out that uncertainty associated with inferred EMIC wave amplitudes from our methods may result from the omittance of some other mechanism(s) that contributes to the proton precipitation, e.g., field line curvature scattering on the night side. The efficiency of this scattering process is controlled by a ratio between the radius of curvature of the magnetic field line and the proton gyroradius. The curvature scattering rates decrease when the ratio increases. When such a ratio exceeds certain threshold level (e.g., ~8), e.g., inside the geostationary orbit, the curvature scattering rates generally become very weak compared to the rates of scattering driven by wave-particle interactions. However, the effect of curvature scattering should be taken into account when POES proton fluxes are measured at higher *L*-shells, e.g., in the central plasma sheet and beyond, as shown in Fig. 5(d)–(e), which requires future investigations.

While this study, as a first step, has concentrated on a detailed case study of a rough conjunction between POES satellites and Van Allen Probe A, lasting for ~0.5 h, the developed procedure to infer EMIC wave amplitudes can be applied to any spatial and temporal space as long as enough data points from multiple POES satellites become available. We note that use of the data from the two different proton energy channels, i.e., 30–80 keV and 80–240 keV, generates different values of inferred EMIC wave amplitudes. Such a disparity may result from several factors in association with our model assumptions, including but not limited to, parallel wave propagation, constant electron density, *L*-shell unchanged wave spectral property and wave normal angle distribution, fixed proton distribution function, and focus on $He^+$ band EMIC waves for simplicity. It tends to be the case that using the POES proton flux data of 30–80 keV energy channel can produce inferred EMIC wave intensities closer to realistic values, since EMIC waves are more likely to resonate with protons at these lower energies (e.g., Summers, 2005; Cao et al., 2016). By performing a simple analysis to compute the resonant proton energy corresponding to the peak wave frequency of adopted $He^+$ band EMIC wave spectrum, we have found that the resonant proton energy for the dominant first-order resonance is ~41 keV, well within the 30–80 keV proton energy channel, which at least partially explain the reason that the 30–80 keV energy channel can provide better agreement with the Van Allen Probe A wave observations than the 80–240 keV energy channel. A comprehensive parametric analysis of the dependence of inferred EMIC wave amplitude on input parameters (e.g., ambient electron density, wave frequency spectrum, wave normal angle distribution, proton energy spectrum) is left as a future study.

## Acknowledgements

This work was supported by NSFC grants 41474141, 41204120, 41674163, 41304130, 41574160, and a grant contract from the National Space Science Center of Chinese Academy of Sciences.

## References

Albert, J.M., Bortnik, J., 2009. Nonlinear interaction of radiation belt electrons with electromagnetic ion cyclotron waves. Geophys. Res. Lett. 36, L12110. http://dx.doi.org/10.1029/2009GL038904.

Anderson, B.J., Erlandson, R.E., Zanetti, L.J., 1992. A statistical study of Pc1–2 magnetic pulsations in the equatorial magnetosphere: 1. Equatorial occurrence distributions. J. Geophys. Res. 97 (A3), 3075–3088. http://dx.doi.org/10.1029/91JA02706.

Cao, X., Ni, B., Liang, J., Xiang, Z., 2016. Resonant scattering of central plasma sheet protons by multiband EMIC waves and resultant proton loss timescales. J. Geophys. Res. Space Phys. 121, 1219–1232. http://dx.doi.org/10.1002/2015JA021933.

Cornwall, J.M., 1965. Cyclotron instabilities and electromagnetic emission in the ultra emission in the ultra low frequency and very low frequency ranges. Geophys. Res. 70 (1), 61–69. http://dx.doi.org/10.1029/JZ070i001p00061.

Criswell, D.R., 1969. Pc 1 micropulsation activity and magnetospheric amplification of 0.2 to 5.0 Hz hydromagnetic waves. J. Geophys. Res. 74 (1), 205–224. http://dx.doi.org/10.1029/JA074i001p00205.

De Soria-Santacruz, M., Li, W., Thorne, R.M., Ma, Q., Bortinik, J., Ni, B., Kletzing, C.A., Kurth, W.S., Hospodarsky, G.B., 2015. Analysis of plasmaspheric hiss wave amplitudes inferred from low-altitude POES electron data: validation with conjunctive Van Allen Probes observations. J. Geophys. Res. Space Phys. 120, 8681–8691. http://dx.doi.org/10.1002/2015JA021148.

Evans, D.S., Greer, M.S., 2004. Polar Orbiting Environmental Satellite Space Environment Monitor-2: Instrument Descriptions and Archive Data Documentation Archive Data Documentation. NOAA Tech. Mem. 93, Version 1.4. Space Weather Predict. Cent., Boulder, Colo.

Fraser, B.J., Grew, R.S., Morley, S.K., Green, J.C., Singer, H.J., Loto'aniu, T.M., Thomsen, M.F., 2010. Storm time observations of

electromagnetic ion cyclotron waves at geosynchronous orbit: GOES results. J. Geophys. Res. 115, A05208. http://dx.doi.org/10.1029/2009JA014516.

Glauert, S.A., Horne, R.B., 2005. Calculation of pitch angle and energy diffusion coefficients with the PADIE code. Geophys. Res. Lett. 110, A04206. http://dx.doi.org/10.1029/2004JA010851.

Horne, R.B., Thorne, R.M., 1997. Wave heating of $He^+$ by electromagnetic ion cyclotron waves in the magnetosphere: heating near the $H^+$-$He^+$ bi-ion resonance frequency. J. Geophys. Res. 102 (11), 457–471. http://dx.doi.org/10.1029/97JA00749.

Jordanova, V.K., Albert, J., Miyoshi, Y., 2008. Relativistic electron precipitation by EMIC waves from self-consistent global simulations. J. Geophys. Res. 113, A00A10. http://dx.doi.org/10.1029/2008JA013233.

Kennel, C.F., Petschek, H.E., 1966. Limit on stably trapped particle fluxes. J. Geophys. Res. 71 (1), 1–28. http://dx.doi.org/10.1029/JZ071i001p00001.

Kurth, W.S., De Pascuale, S., Faden, J.B., Kletzing, C.A., Hospodarsky, G.B., Thaller, S., Wygant, J.R., 2015. Electron densities inferred from plasma wave spectra obtained by the waves instrument on Van Allen Probes. J. Geophys. Res. Space Phys. 120, 904–914. http://dx.doi.org/10.1002/2014JA020857.

Lam, M.M., Horne, R.B., Meredith, N.P., Glauert, S.A., Moffat-Griffin, T., Green, J.C., 2010. Origin of energetic electron precipitation >30 keV into the atmosphere. J. Geophys. Res. 115, A00F08. http://dx.doi.org/10.1029/2009JA01461.

Liu, K., Lemons, D.S., Winske, D., Gary, S.P., 2010. Relativistic electron scattering by electromagnetic ion cyclotron fluctuations: test particle simulations. J. Geophys. Res. 115, A04204. http://dx.doi.org/10.1029/2009JA014807.

Li, W., Ni, B., Thorne, R.M., Bortnik, J., Green, J.C., Kletzing, C.A., Kurth, W.S., Hospodarsky, G.B., 2013. Constructing the global distribution of chorus wave intensity using measurements of electrons by the POES satellites and waves by the Van Allen Probes. Geophys. Res. Lett. 40, 4526–4532. http://dx.doi.org/10.1002/grl. 50920.

Loto'aniu, T.M., Thorne, R.M., Fraser, B.J., Summers, D., 2006. Estimating relativistic electron pitch-angle scattering rates using properties of the electromagnetic ion cyclotron wave spectrum. J. Geophys. Res. 111, A04220. http://dx.doi.org/10.1029/2005JA011452.

Meredith, N.P., Horne, R.B., Lam, M.M., Denton, M.H., Borovsky, J.E., Green, J.C., 2011. Energetic electron precipitation during high-speed solar wind stream driven storms. J. Geophys. Res. 116, A05223. http://dx.doi.org/10.1029/2010JA016293.

Ni, B., Li, W., Thorne, R.M., Bortnik, J., Green, J.C., Kletzing, C.A., Kurth, W.S., Hospodarsky, G.B., Soria-Santacruz Pich, M., 2014. A novel technique to construct the global distribution of whistler mode chorus wave intensity using low-altitude POES electron data. J. Geophys. Res. Space Phys. 119, 5685–5699. http://dx.doi.org/10.1002/2014JA019935.

Ni, B., Cao, X., Zou, Z.Y., Zhou, C., Gu, X.D., Bortnik, J., 2015. Resonant scattering of outer zone relativistic electrons by multiband EMIC waves and resultant electron loss time scales. J. Geophys. Res. Space Phys. 120, 7357–7373. http://dx.doi.org/10.1002/2015JA021466.

Rodger, C.J., Clilverd, M.A., Green, J.C., Lam, M.M., 2010. Use of POES SEM-2 observations to examine radiation belt dynamics and energetic electron precipitation into the atmosphere. J. Geophys. Res. 115, A04202. http://dx.doi.org/10.1029/2008JA014023.

Roux, A., Perraut, S., Rauch, J., De Villedary, C., Kremser, G., Korth, A., Young, D., 1982. Wave-particle interactions near $\Omega He^+$ observed on board GEOS 1 and 2: 2. Generation of ion cyclotron waves and heating of $He^+$ ions. J. Geophys. Res. 87 (A10), 8174–8190. http://dx.doi.org/10.1029/JA087iA10p08174.

Santolík, O., Parrot, M., Lefeuvre, F., 2003. Singular value decomposition methods for wave propagation analysis. Radio Sci. 38 (1), 1010. http://dx.doi.org/10.1029/2000RS002523.

Summers, D., Thorne, R.M., 2003. Relativistic electron pitch-angle scattering by electromagnetic ion cyclotron waves during geomagnetic storms. J. Geophys. Res. 108 (A4), 1143. http://dx.doi.org/10.1029/2002JA009489.

Summers, D., 2005. Quasi-linear diffusion coefficients for field-aligned electromagnetic waves with applications to the magnetosphere. J. Geophys. Res. 110, A08213. http://dx.doi.org/10.1029/2005JA011159.

Summers, D., Ni, B., Meredith, N.P., 2007. Timescales for radiation belt electron acceleration and loss due to resonant wave-particle interactions: 1. Theory. J. Geophys. Res. 112, A04206. http://dx.doi.org/10.1029/2006JA011801.

Thorne, R.M., Horne, R., 1992. The contribution of ion-cyclotron waves to electron heating and SAR-arc excitation near the storm-time plasmapause. Geophys. Res. Lett. 19, 417–420. http://dx.doi.org/10.1029/92GL0089.

Thorne, R.M., 2010. Radiation belt dynamics: the importance of wave-particle interactions. Geophys. Res. Lett. 37, L22107. http://dx.doi.org/10.1029/2010GL1044990.

Thorne, R.M., Li, W., Ni, B., Ma, Q., Bortnik, J., Chen, L., Baker, D.N., Spence, H.E., Reeves, G.D., Henderson, M.G., Kletzing, C.A., Kurth, W.S., Hospodarsky, G.B., Blake, J.B., Fennell, J.F., Claudepierre, S. G., Kanekal, S.G., 2013. Rapid local acceleration of relativistic radiation-belt electrons by magnetospheric chorus. Nature 504, 411–414. http://dx.doi.org/10.1038/nature12889.

Ukhorskiy, A.Y., Shprits, Y.Y., Anderson, B.J., Takahashi, K., Thorne, R.M., 2010. Rapid scattering of radiation belt electrons by storm-time EMIC waves. Geophys. Res. Lett. 37, L09101. http://dx.doi.org/10.1029/2010GL042906.

Wang, Q., Cao, X., Gu, X., Ni, B., Zhou, C., Shi, R., Zhao, Z., 2016. A parametric study of the linear growth of magnetospheric EMIC waves in a hot plasma. Phys. Plasmas 23 (6), 062903.

Xiao, F., Yang, C., Zhou, Q., He, Z., He, Y., Zhou, X., Tang, L., 2012. Nonstorm time scattering of ring current protons by electromagnetic ion cyclotron waves. J. Geophys. Res. 117, A08204. http://dx.doi.org/10.1029/2012JA017922.

Xiao, F., Yang, C., Su, Z., Zhou, Q., He, Z., He, Y., Baker, D.N., Spence, H.E., 2015. Wave-driven butterfly distribution of Van Allen belt relativistic electrons. Nat. Commun. 6. http://dx.doi.org/10.1038/ncomms9590.